GT2023-101460

REAL-TIME PARAMETER INFERENCE OF NONLINEAR BLUFF-BODY-STABILIZED FLAME MODELS USING BAYESIAN NEURAL NETWORK ENSEMBLES

Maximilian L. Croci[1], Ushnish Sengupta[1], Ekrem Ekici[1], Matthew P. Juniper[1,*]

[1]University of Cambridge, Cambridge, United Kingdom

ABSTRACT

We assimilate the parameters of a low order physics-based model of a bluff-body-stabilized premixed flame by observing OH PLIF and PIV images of a 1.1 MW flame. The model is a five parameter level set (G-equation) solver with a prescribed velocity field. A Bayesian ensemble of neural networks (BayNNE) is trained on numerical simulations of the model at 2400 different parameter combinations. Once trained, the BayNNE observes the experimental data and outputs the expected values and uncertainties of the parameters of the model that best fits the experimental data. Using this model, we extrapolate the heat release rate field in physical space beyond the observed window in the experiments, and in parameter space to smaller perturbation amplitudes. We then convert the periodic heat release rate field into a distributed $n - \tau$ model, which we enter into a thermoacoustic Helmholtz solver. We find that the thermoacoustic eigenvalue drift is small but measurable, is stabilizing, and does not vary significantly during the experimental run or with the velocity amplitude. This is primarily because the time delay field τ, which is determined by the convection speed, is similar for all cases. This is consistent with the experimental images, which exhibit intermittent bouts of thermoacoustic oscillations that die away. Although this paper's conclusions for thermoacoustic behaviour are unsurprising, the method it describes is a potentially cheap way to combine sparse experimental measurements with copious low order simulations.

Keywords: Thermoacoustics, Neural Networks, Machine Learning, Data Assimilation, Flame Transfer Function

1. INTRODUCTION

The modelling, prediction, and control of thermoacoustic instability is a persistent challenge in jet and rocket engine design. This is because the thermoacoustic behaviour of these engines is exceedingly sensitive to small changes in design or operating point [1]. Any errors in thermoacoustic models can therefore have a strong influence on the predicted thermoacoustic behaviour. Choosing a good model is challenging because high order models can be too expensive, while low order models can be too inaccurate. This is particularly challenging when modelling industrial thermoacoustic systems that contain turbulent flames.

Recently, advances in experimental diagnostics and in computational power have led to vast quantities of data becoming available. The question is how best to use this data. All approaches, whether data-driven or physics-based, involve assimilating data into models. In many data-driven approaches, the model is a neural network (NN) containing millions of parameters. The NN is a versatile model that can model anything, without knowledge of the physics. Its parameters are found by minimizing the discrepancy between the model prediction and the data, meaning that it learns to interpolate between the data it has already seen. In physics-based approaches, on the other hand, the model is a qualitatively-accurate model of the underlying physics, containing parameters that are learned from the data. When performed rigorously [2], the user specifies the prior expected values and uncertainties in the parameters before assimilating the data, assigns some uncertainty to the data, and then calculates the posterior expected values and uncertainties of the parameters. For a field such as thermoacoustics, which has been accumulating physics-based knowledge for over a century, it seems absurd to discard this knowledge in favour of a purely data-driven approach involving NNs. Nevertheless, it is worth investigating the potential benefits that the data-driven approach, and associated tools, can bring to the field.

In situations in which the physics is unknown or unmodellable, pure data-driven approaches work well. For example, a NN can be trained to recognize the decay rate of thermoacoustic oscillations in a tube containing a turbulent flame, given only the noise of the undisturbed turbulent flame [3]. In this case, the physics relating the noise to the flame shape, and then the flame shape to the thermoacoustic behaviour, would be difficult to model. Instead, the NN simply learns the relationship between noise and thermoacoustic behaviour from data, providing a useful prognosis tool. This tool has been extended to full-scale aircraft engines [4] and to laboratory-scale rocket engines [5]. In each

case, it gives around 0.5 seconds warning of impending thermoacoustic instability, which would be sufficient to take evasive action.

In situations in which the physics is known and can be modelled, a NN contains too many unknown parameters to be an appropriate tool. It is more efficient and more informative to propose qualitatively-accurate physics-based models and to assimilate their parameters from experimental data using Bayesian inference [6]. When performed rigorously, the posterior parameter uncertainties are also assimilated, which allows the researcher to compare physics-based models against each other, to penalize models with too many parameters, and to discover which candidate model is most likely to explain a given set of data. Unlike NNs, these physics-based models can extrapolate into physical space and parameter space that has not been observed, as long as the physics remains unchanged and the models remain valid.

This paper follows the physics-based approach but does not use the conventional Bayesian method, a Kalman filter [7], to assimilate the model parameter values and their uncertainties. Instead it uses a Bayesian ensemble of neural networks (BayNNE) to assimilate the model parameters and their uncertainties. This combines the attractive features of physics-based approaches, such as extrapolatability and interpretability, with the attractive features of NNs, such as speed and ease of use. We focus mainly on the flame behaviour, which is usually the hardest part of a thermoacoustic system to model. We extrapolate the flame behaviour in physical and parameter space and then investigate how this influences the predicted thermoacoustic behaviour of the system.

1.1 The thermoacoustic mechanism and flame modelling

Thermoacoustic instabilities grow when heat release rate oscillations and pressure oscillations are sufficiently in phase [8]. Heat release rate fluctuations are caused by flame surface area fluctuations, which in turn are caused by velocity perturbations and flame dynamics [9–13]. Any physics-based model of a gas-turbine flame must therefore contain the flame's response to velocity perturbations. In addition, equivalence ratio perturbations must also be included for partially-premixed or spray flames.

In the simplest physics-based flame model, the heat release rate fluctuation is a linear multiple, n, of the velocity perturbation at the base of the flame some time τ earlier. This is known as the lumped $n - \tau$ model [14]. This model is too simple for our purposes because it does not simulate the flame dynamics. In this paper we model the flame as the zero contour (or level-set) of a continuous function that advects with the flow and propagates normal to the zero contour. This is known as the G-equation model [15] and it allows the most influential flame dynamics to be simulated cheaply. These fluctuations can then be expressed as a distributed $n - \tau$ model [16], in which n and τ have the same meaning as before, but are distributed in space.

1.2 Bayesian deep learning

In this paper, the parameters of the flame model are assimilated from experimental data. The experimental data comes from high frequency OH planar laser induced fluorescence (OH PLIF) measurements of the turbulent flame in a 1.1 MW version of the Volvo combustor rig [17]. Previously, we used the ensemble
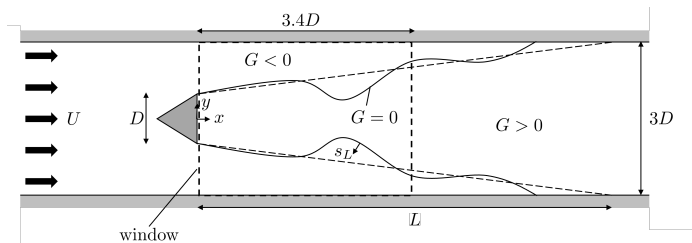

FIGURE 1: DIAGRAM OF THE VOLVO COMBUSTOR AND G-EQUATION MODEL OF THE FLAME. THE FLAME BURNS PREMIXED AIR AND PROPANE, STABILIZED ON A TRIANGULAR BLUFF BODY. THE FLAME FRONT IS REPRESENTED BY THE $G = 0$ CONTOUR OF A CONTINUOUS SCALAR FIELD $G(x, y, t)$.

Kalman filter [18] (EnKF) to assimilate data from a bunsen flame into this G-equation model [19, 20]. The EnKF infers the parameters of the G-equation model by combining model forecasts with experimental measurements within a Bayesian framework. However, the computational requirements of the EnKF make real-time Bayesian inference unfeasible when measurements are taken at high frequency. Furthermore, we have found that the method sometimes fails to infer parameters when they vary quickly in time, and suffers from numerical instability when the measurements are noisy or the behaviour changes abruptly. For these reasons the Kalman filter is not suitable for assimilation of these experimental images.

Instead, we use an ensemble of Bayesian neural networks. Bayesian deep learning refers to the use of deep learning algorithms, such as deep artificial neural networks (NNs), for Bayesian inference [21]. Bayesian NNs [2] replace the point estimates of each of the NN's weights and biases with Gaussian probability distributions, with means and variances learned during training. The distribution of every weight and bias in the NN can be used to infer the outputs from the inputs. For example the parameters of a model can be inferred from experimental measurements. Bayesian NNs of practical size are, however, too expensive to train [21]. More recently, ensembles of deep NNs have been used to perform approximate Bayesian inference [22–24]. The approximation improves as the width of the NN's hidden layers increases. These Bayesian NN ensembles (BayNNEs) learn the mean and variance of the posterior distribution of the outputs given the inputs. When multiple outputs are to be inferred, heteroscedastic BayNNEs learn the means and variances of each output, without assuming a common variance for all outputs. This study uses heteroscedastic BayNNEs to infer the parameters of the G-equation model of a bluff-body stabilised flame given experimental observations [25, 26].

2. EXPERIMENTAL DATA AND IMAGE PROCESSING

The flame images are from experiments performed on a version of the Volvo combustor [17, 28, 29] shown schematically in Figure 1. Premixed air and propane flow into the combustor and are burnt by a flame stabilized on a triangular bluff body with side length $D = 3.8$ cm. The heat release rate is 1.1 MW. As the air-fuel mixture flows through the combustor, vortices are shed periodically from the bluff body. These vortices cause wrinkling
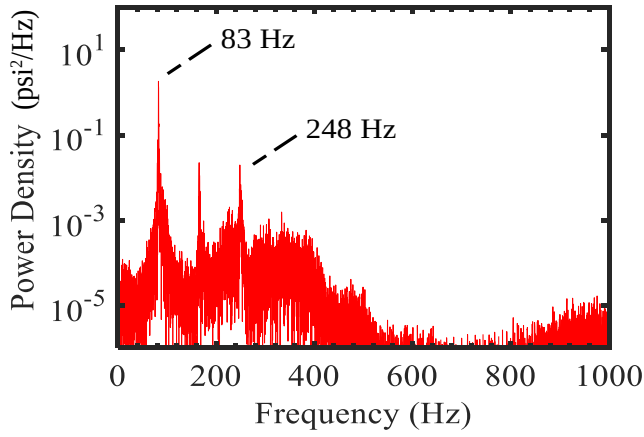
FIGURE 2: POWER SPECTRAL DENSITY OF THE SIGNAL FROM A HIGH-FREQUENCY PRESSURE TRANSDUCER IN THE RIG, FROM REF. [27].
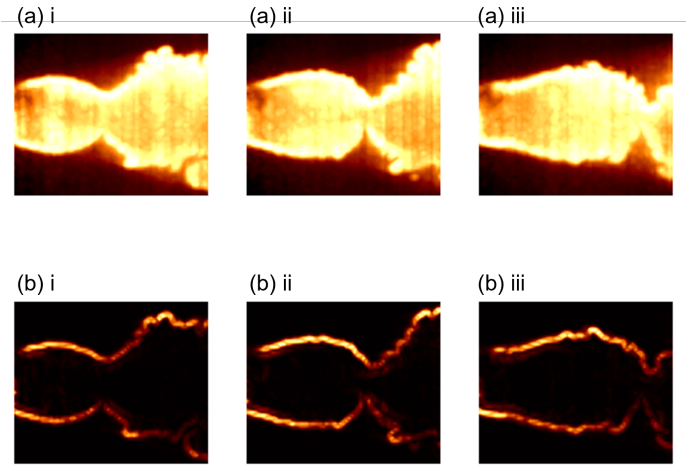

FIGURE 3: *(A)* PLOTS OF OH PLANAR LASER INDUCED FLUORESCENCE (OH PLIF) INTENSITY IMAGES OF THE FLAME TAKEN THROUGH THE OBSERVATION WINDOW. *(B)* PLOTS OF THE MAGNITUDE OF THE GRADIENT VECTOR OF OH INTENSITY, INDICATING THE FLAME FRONT [17].

and cusping of the flame front. In addition to this motion, a large scale varicose mode exists intermittently with a period of 83 Hz (Fig. 2), which is near the fundamental acoustic frequency of the combustor. We wish to assimilate data into a model for this mode. 8000 images of the flame such as those in Fig. 3(a) are recorded at 10kHz using OH planar laser induced fluorescence (OH PLIF) through a window $3D$ tall and $3.4D$ wide. Simultaneous PIV is also recorded. In this paper we examine an experimental run at a single operating point. We have equivalent images from one other operating point, in which the varicose mode is not present. Our model is designed to assimilate data from the varicose mode, so the data from the other operating point was not relevant.

The images are processed to find the position $y = f(x)$ of the flame front by thresholding and interpolating the magnitude of the OH gradient vector at each point, as shown in Fig. 3(b). The vectors of positions $\mathbf{y}$ are smoothed using splines with 10 knots. Ten position vectors are appended to form a column vector, $\mathbf{z}$, representing a sequence of 10 flame front positions. We refer to column vectors $\mathbf{z}$ as observation vectors.

3. ASSIMILATION INTO A FLAME MODEL

3.1 The flame model

The flame front is modelled as a thin boundary between unburnt and burnt gases (Fig. 1). In this model, the flame travels normal to itself into the unburnt gases with laminar flame speed s_L, which depends on the gas composition. The velocity of the burnt gases does not affect the flame kinematics. The unburnt and burnt gases are assumed to travel with velocity $\mathbf{u}(x, y, t)$. Under these assumptions, the flame front is modelled by the $G(x, y, t) = 0$ contour (or level-set) of a continuous scalar field G, whose motion is governed by the G-equation:

$$\frac{\partial G}{\partial t} + \mathbf{u} \cdot \nabla G = s_L |\nabla G|. \tag{1}$$

The flow velocity field $\mathbf{u}$ is modelled as the superposition of a uniform and constant base flow, U, and a continuity-obeying velocity perturbation, $u'(x, t)$ and $v'(x, y, t)$:

$$\frac{\mathbf{u}(x, y, t)}{U} = (1 + u'(x, t))\,\mathbf{i} + v'(x, y, t)\mathbf{j}, \tag{2}$$

$$u'(x, t) = \varepsilon \left(\frac{x}{D}\right)^{\gamma} \sin\left(\mathrm{St}\left(K\left(\frac{x}{D}\right) - t\right)\right), \tag{3}$$

$$
\begin{aligned}
v'(x, y, t) =\; & \varepsilon\gamma \left(\frac{x}{D}\right)^{\gamma-1} \left(\frac{y}{D}\right) \sin\left(\mathrm{St}\left(K\left(\frac{x}{D}\right) - t\right)\right) \\
& - \mathrm{St}K\varepsilon \left(\frac{x}{D}\right)^{\gamma} \left(\frac{y}{D}\right) \cos\left(\mathrm{St}\left(K\left(\frac{x}{D}\right) - t\right)\right),
\end{aligned}
\tag{4}
$$

where U is a characteristic speed, ε is a non-dimensional amplitude, St is the Strouhal number of the flame with characteristic length D, excitation frequency f, and nominal aspect ratio β: $\mathrm{St} = 2\pi f \beta D/U$, and K is the ratio of the characteristic speed U to the perturbation phase speed, v_p. The parameter γ is introduced to the flame perturbation model to allow for the horizontal velocity perturbations to increase in size with distance from the flame holder, which is the qualitative behaviour observed in the experiment. This has proven to be a versatile flame front model in several previous studies, despite having only a few parameters [30]. To make the G-equation model quantitatively accurate, the parameters $K, \varepsilon, \gamma, \mathrm{St}$ and β must be tuned to fit an observed flame shape.

3.2 The library of simulated flame fronts

For the simulations we use LSGEN2D [31], which is a level-set solver that iterates the G field of the G-equation model for known parameters $K, \varepsilon, \gamma, \mathrm{St}$ and β. In this study, the G field is iterated forward in time for a duration of 5 periods, where the period is $1/f$. This allows any transient flame behaviour to decay. Then the G field is iterated for a further period. The value of the G field at $N_T = 200$ equally spaced time steps within this period is recorded: $\{G_1, G_2, \ldots, G_{N_T}\}$. For each G

3

field in the sequence $\{G_i\}$, the flame edge $y = f(x)$ is extracted from the $G = 0$ contour for all x in the range of the experiment observation window. The flame edge y coordinates are recorded in a column vector $\mathbf{y}_i$. The resulting sequence $\{\mathbf{y}_1, \mathbf{y}_2, \ldots, \mathbf{y}_{N_T}\}$ represents the flame edge position at N_T equally spaced time steps in the period. The frame rate of this sequence is N_T/T which is not, in general, equal to the frame rate of the experimental data ($f_s = 10^4$ Hz). To create a sequence of 10 simulated flame edges with the same frame rate as the experimental data starting from a time step t_1, we calculate the ratio $\Delta = N_T f/f_s$ and select the sequence $\{\mathbf{y}_{t_1}, \mathbf{y}_{t_1+\Delta}, \ldots, \mathbf{y}_{t_1+9\Delta}\}$. The vectors in this sequence are appended to make a column vector $\mathbf{z}$. This is repeated for all N_T of the starting time steps $t_1, t_2 \ldots t_{N_T}$, and for $P = 2400$ combinations of parameters sampled from the ranges shown in Table 1. The result is a library of $PN_T = 4.8 \times 10^5$ observation - parameter pairs.

3.3 The heteroscedastic Bayesian neural network ensembles

The posterior probability distribution $p(\mathbf{p}|\mathbf{z})$ of the G-equation parameters $\mathbf{p}$, given the observations $\mathbf{z}$ is assumed to be a multivariate Gaussian with mean vector $\boldsymbol{\mu}(\mathbf{z})$ and diagonal covariance matrix $\boldsymbol{\Sigma}(\mathbf{z}) = \text{diag}(\boldsymbol{\sigma}^2(\mathbf{z}))$. An ensemble of M neural networks are trained on the simulated flame front library to predict the mean and variance vectors, $\boldsymbol{\mu}(\mathbf{z})$ and $\boldsymbol{\sigma}^2(\mathbf{z})$. Each neural network in the ensemble produces estimates $\boldsymbol{\mu}_j(\mathbf{z}_i)$ and $\boldsymbol{\sigma}_j^2(\mathbf{z}_i)$ for each observation vector $\mathbf{z}_i$. These estimates are combined following Ref. [32] as:

$$\boldsymbol{\mu}(\mathbf{z}_i) = \frac{1}{M} \sum_j \boldsymbol{\mu}_j(\mathbf{z}_i), \tag{5}$$

$$\boldsymbol{\sigma}^2(\mathbf{z}_i) = \frac{1}{M} \sum_j \boldsymbol{\sigma}_j^2(\mathbf{z}_i) + \frac{1}{M} \sum_j \boldsymbol{\mu}_j^2(\mathbf{z}_i) - \boldsymbol{\mu}^2(\mathbf{z}_i), \tag{6}$$

Each neural network comprises 4 fully connected layers 600 hidden units wide, and two output layers (one for the mean vector, one for the variance vector) each 6 units wide. ReLU activations are used for the hidden layers, a sigmoid activation is used for the output layer for the mean and an exponential activation is used for the variance layer, to ensure positivity. The architecture of one such neural network is shown in Fig. 4.

The weights $\boldsymbol{\theta}_j$ of each neural network are initialised by sampling from Gaussian prior distributions with means $\mathbf{0}$ and covariance matrices $\boldsymbol{\Sigma}_{prior}$ according to He normalisation[33]. During training, the weights are anchored to their initial values
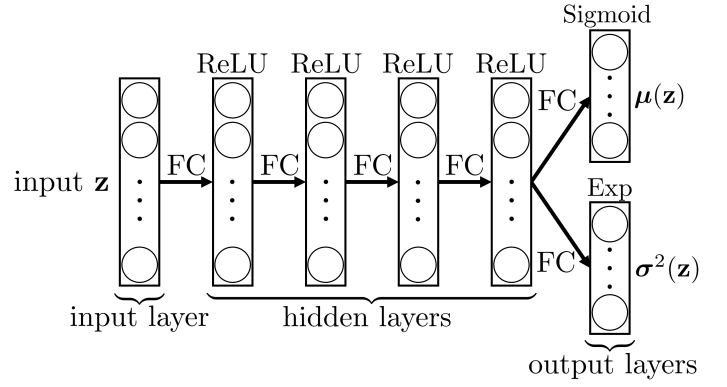

FIGURE 4: ARCHITECTURE OF EACH NEURAL NETWORK IN THE ENSEMBLE OF 20. THE INPUT AND HIDDEN LAYERS HAVE 600 UNITS EACH, WHILE EACH OUTPUT LAYER HAS 6 UNITS EACH. ALL LAYERS ARE FULLY CONNECTED (FC). RECTIFIED LINEAR UNIT (RELU) ACTIVATION FUNCTIONS ARE USED FOR THE HIDDEN LAYERS AND SIGMOID AND EXPONENTIAL (EXP) ACTIVATION FUNCTIONS ARE USED FOR THE MEAN AND VARIANCE OUTPUT LAYERS RESPECTIVELY.

$\boldsymbol{\theta}_{j,anc}$. The loss function used for training is:

$$\mathcal{L}_j = (\boldsymbol{\mu}_j(\mathbf{z}) - \mathbf{p})^T \boldsymbol{\Sigma}_j(\mathbf{z})^{-1} (\boldsymbol{\mu}_j(\mathbf{z}) - \mathbf{p}) + \log(|\boldsymbol{\Sigma}_j(\mathbf{z})|)$$
$$+ (\boldsymbol{\theta}_j - \boldsymbol{\theta}_{anc,j})^T \boldsymbol{\Sigma}_{prior}^{-1} (\boldsymbol{\theta}_j - \boldsymbol{\theta}_{anc,j}). \tag{7}$$

This is constructed by adding a regularization term to the weights (third term of $\mathcal{L}_j$) to the negative log-likelihood of the parameter predictions (first two terms of $\mathcal{L}_j$). Training the ensemble with this loss function is known as Bayesian ensembling with maximum a-posteriori (MAP) sampling. It is a general method which can be used to infer a Bayesian posterior to uncorrelated target variables. The loss function encourages the BayNNE to learn both accurate parameter predictions and their uncertainties, which is a sensible objective in applications where aleatoric and epistemic uncertainties arise.

An ensemble of size $M = 20$ is trained for 100 epochs on a Tesla P100 GPU on Google Colab[1]. This takes approximately 3 hours. Once converged, the ensemble is evaluated on the observations, which takes milliseconds.

3.4 Parameter estimation from the BayNNE and modelled flame behaviour

Each flame front position vector appears in 10 consecutive observation vectors. There are therefore 10 sets of ensemble parameter predictions for each timestep. For each timestep, the re-simulated flame is a weighted average of the flames re-simulated with the 10 sets of parameters. Greater weight is given to flames re-simulated using parameters predicted from an observation vector in which the flame front position vector appears in the middle of the observation vector.

We assimilate the data from all 8000 timesteps. At each timestep, the BayNNE recognises the parameters (K, ε, γ, St, β) of the simulations that best match this experimental data and

---

[1]Google Colaboratory ("Colab") is a Jupyter notebook environment for interactive development, https://colab.research.google.com/.
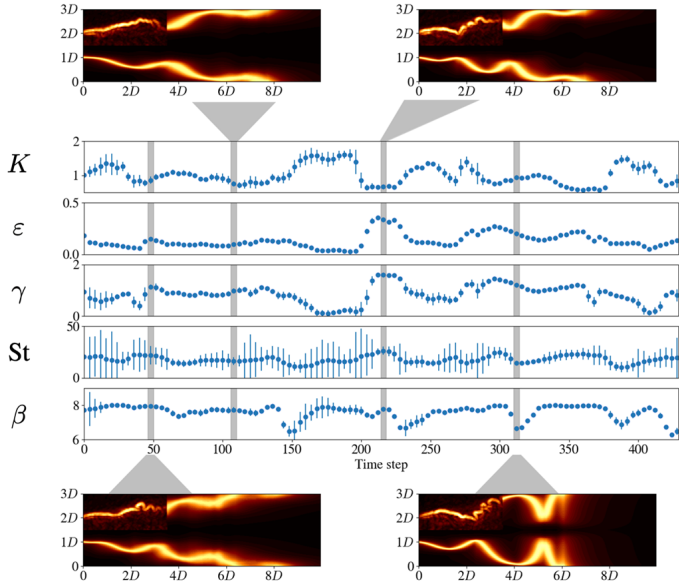
FIGURE 5: EXPERIMENTAL FLAME IMAGES (TOP-LEFT QUAD-
RANT OF EACH IMAGE) AND LEVEL-SET MODEL PREDICTIONS
(REMAINDER OF IMAGE) AT FOUR TIMESTEPS WITHIN A SE-
QUENCE OF 430 TIMESTEPS. THE GRAPHS SHOW THE MEANS
AND ± 2 STANDARD DEVIATIONS OF THE FIVE PARAMETERS OF
THE G-EQUATION SIMULATION, AFTER ASSIMILATION FROM THE
EXPERIMENTAL DATA. THE LEVEL-SET MODEL PREDICTIONS
USE THESE ASSIMILATED VALUES TO SIMULATE THE FLAME
DOWNSTREAM, BEYOND THE OBSERVATION WINDOW. THE IN-
FERRED PARAMETER VALUES ARE LISTED IN TABLE 2.

also outputs the uncertainty in those parameters, in the form of
a standard deviation. The expected values and two standard de-
viations are shown in Fig. 5 for 430 of the 8000 timesteps. The
BayNNE is certain about some parameters, such as K, ε, γ, and
β, but, when the flame behaviour is far from periodic, is uncer-
tain about St. The parameter values tend to remain approximately
constant for many timesteps and then change abruptly. This con-
curs with a visual inspection of the experimental data which also
exhibits periods of similar behaviour interspersed with moments
of abrupt change. The BayNNE is able to assimilate the data
reliably through these abrupt changes, while the EnKF[20] is not.

The varicose mode that we assimilate is intermittent so is
present for some blocks of timesteps but not others. In Fig. 5 we
show the assimilated parameters from 430 of the 8000 timesteps
and highlight four timesteps in which the varicose mode can be
observed particularly well. The top-left quadrant of the four flame
images in Fig. 5 shows the experimental flame position (Fig. 3)
at that timestep in the experimental run.

At each stage, parameter samples from the posterior distri-
bution inferred from the BayNNE are entered into G-equation
simulations to create a distribution of flame positions and heat
release rate fluctuations in space and time. This converts the un-
certainty in the flame positions into a distributed heat release rate
field. The heat release rate fields match the flame observations
well within the observed window, and also extrapolate beyond the
window. We emphasise that this extrapolation is achieved using
the physics-based flame front model, and not using the BayNNE;

the BayNNE has been used only to identify the parameters from
the images in the window.

The parameters are inferred from large amplitude flame os-
cillations but, in later sections of this paper, we investigate how
the flame would behave at lower amplitudes. We therefore repeat
the above calculations at the same parameter values, but with
smaller values of the velocity field amplitude ε (Tab. 1). These
amplitudes are $\varepsilon/4$, $\varepsilon/2$, and $3\varepsilon/4$, where ε is the amplitude as-
similated from the experimental data. This is an extrapolation of
the physics-based G-equation model rather than an extrapolation
of the BayNNEs.

3.5 The flame behaviour expressed as a distributed $n - \tau$ model

The above analysis gives the local heat release rate field,
$q(\mathbf{x}, t)$, and the local velocity field, $u(\mathbf{x}, t)$, over one cycle at a
known frequency, ω, where $\mathbf{x} = (x, y)$. At each pixel, we take
the Fourier transform of q and u at ω, for example $\hat{q}(\mathbf{x}, \omega) = \int q(\mathbf{x}, t) \exp(i\omega t)dt$, and convert this to the heat release rate per
unit volume by dividing by the volume corresponding to each
pixel. The n and τ fields are calculated as follows:

$$n(\mathbf{x}) = \left| \frac{\hat{q}(\mathbf{x}, \omega)}{I} \right| \, , \quad \phi(\mathbf{x}) = \angle \left(\frac{\hat{q}(\mathbf{x}, \omega)}{I} \right) , \quad (8)$$

where $I = \int_{\Omega} w(\mathbf{x})|\hat{u}(\mathbf{x}, \omega)|d\mathbf{x}$ and $w(\mathbf{x})$ is the measurement zone:

$$w(x, y) = \exp\left(-a_r (x - x_0)^2 - a_r (|y| - y_0)^2) \right) , \quad (9)$$

where $a_r = 6200$, and $(x_0, y_0) = (D/2, D)$ where D is the bluff-
body side length. This measurement zone must be the same in
the thermoacoustic model as it is in the heat release model. The
phase, $\phi(\mathbf{x})$, of q is wrapped between $\pm\pi$ and is unwrapped with
the algorithm in Ref. [35]. The phase is then divided by ω to
give the spatially-distributed time delay $\tau(\mathbf{x})$. Finally, the n field

**TABLE 2: PARAMETER VALUES AND UNCERTAINTIES INFERRED
BY THE BAYNNES AT FOUR TIMESTEPS IN FIG./REFFIG:RESULTS.**

Par.	$t = 48$	$t = 108$	$t = 216$	$t = 312$
K	0.95 ± 0.08	0.72 ± 0.08	0.69 ± 0.02	0.93 ± 0.01
ε	0.13 ± 0.01	0.10 ± 0.00	0.31 ± 0.00	0.18 ± 0.00
γ	1.12 ± 0.14	1.01 ± 0.11	1.58 ± 0.02	1.15 ± 0.01
St	21.2 ± 8.4	16.4 ± 5.3	25.7 ± 4.9	14.3 ± 1.9
β	7.93 ± 0.02	7.69 ± 0.12	7.74 ± 0.05	6.71 ± 0.12

**TABLE 3: INTENSITY, η, OF THE GLOBAL TRANSFER FUNCTION
BETWEEN VELOCITY FLUCTUATIONS AND HEAT RELEASE RATE
FLUCTUATIONS (IN JOULES/METRE) [34], AT FOUR DIFFERENT
TIMESTEPS AND FOUR DIFFERENT AMPLITUDES.**

Amplitude	$t = 48$	$t = 108$	$t = 216$	$t = 312$
$\varepsilon/4$	160.7	168.8	258.2	232.1
$\varepsilon/2$	163.6	173.3	265.1	240.0
$3\varepsilon/4$	165.6	174.1	270.1	246.6
ε	167.8	175.2	274.2	252.4

(a) Re-simulated flame

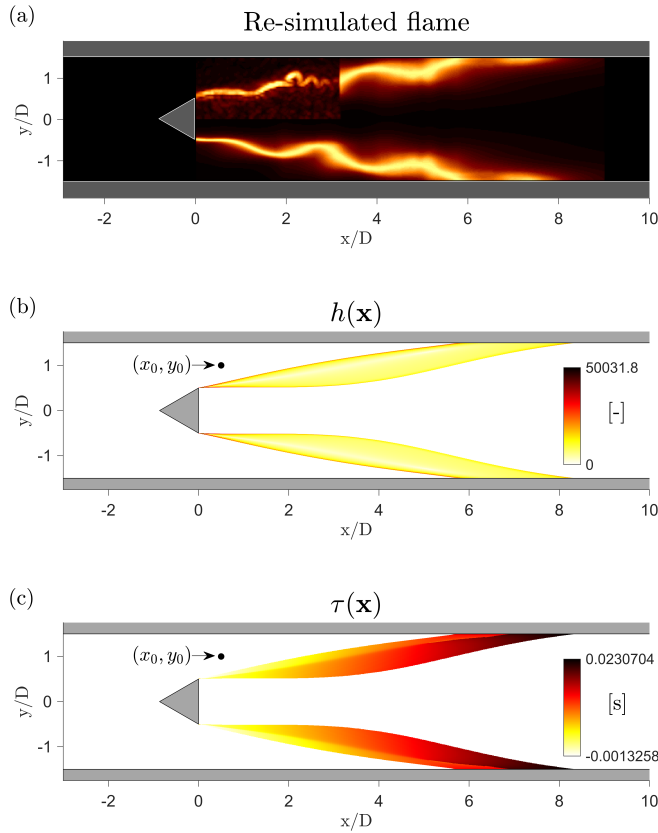(b) $h(\mathbf{x})$

(c) $\tau(\mathbf{x})$

FIGURE 6: (A): RE-SIMULATED FLAME SHAPE AT $t = 48$. (B) AND (C): n AND τ FIELDS CALCULATED FROM THE RE-SIMULATED FLAME SHAPE AT $t = 48$. THE CENTRE (x_0, y_0) OF THE MEASUREMENT REGION $w(x, y)$ IS ALSO SHOWN. PART OF THE FLAME IS UPSTREAM OF THE MEASUREMENT POINT, WHICH LEADS TO A NEGATIVE TIME DELAY.

FIGURE 7: AS FOR FIG. 6 WITH $t = 108$.

FIGURE 8: AS FOR FIG. 6 WITH $t = 216$.

is scaled to a field that integrates to 1 multiplied by a scalar, η, in units of J/m, in order to be consistent with equation [4] of Ref. [34].

The values of η are shown in Tab. 3 at the four highlighted timesteps in Fig. 5 reproduced at the four different amplitudes ε. The corresponding heat release rate distributions and time delay distributions are shown in figures 6 to 11. In the next section, these distributed $n - \tau$ models are included in a thermoacoustic Helmholtz solver to model the thermoacoustic behaviour a system containing these flames.

4. PREDICTED THERMOACOUSTIC BEHAVIOUR

4.1 Themoacoustic Helmholtz solver

The thermoacoustic Helmholtz equations solved in this paper are equations (3–5) in Ref. [34], which are converted to the frequency domain and expressed as a nonlinear eigenvalue problem for the complex angular frequency, s. The unsteady behaviour of the flame is modelled using the local formulation of the $n - \tau$ model in section 3.5 with the same measurement region. This is the approach taken in [16, 34, 36]. The temperature distribution
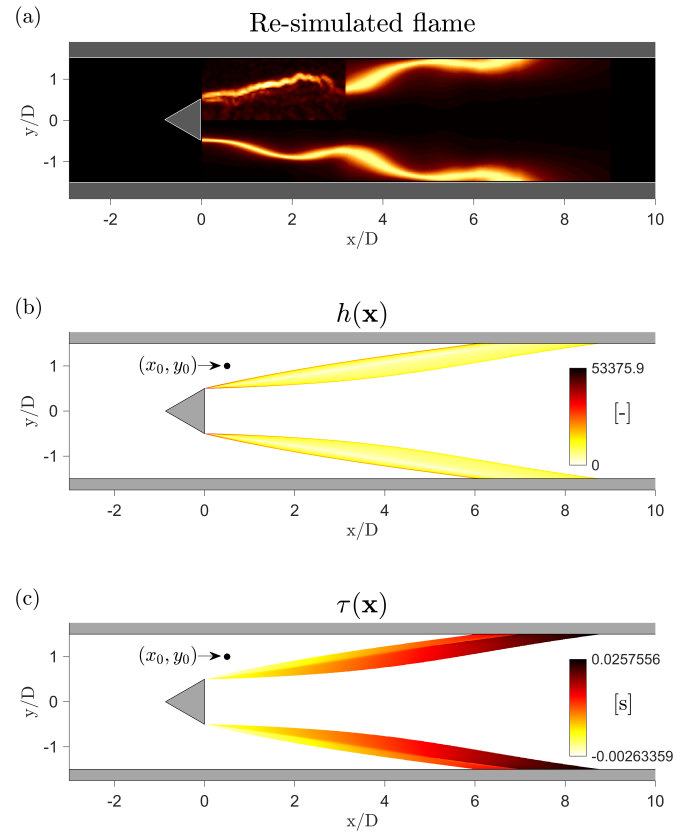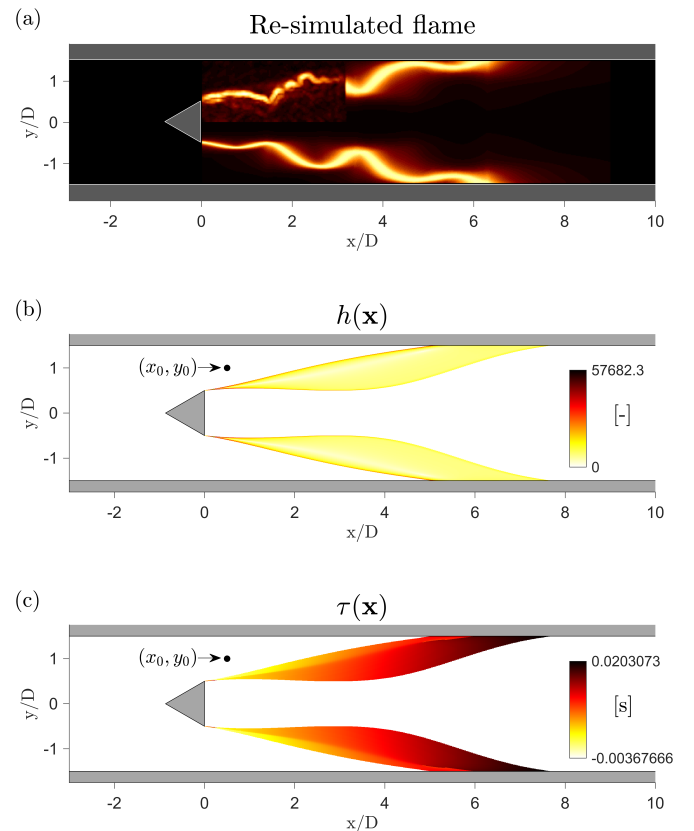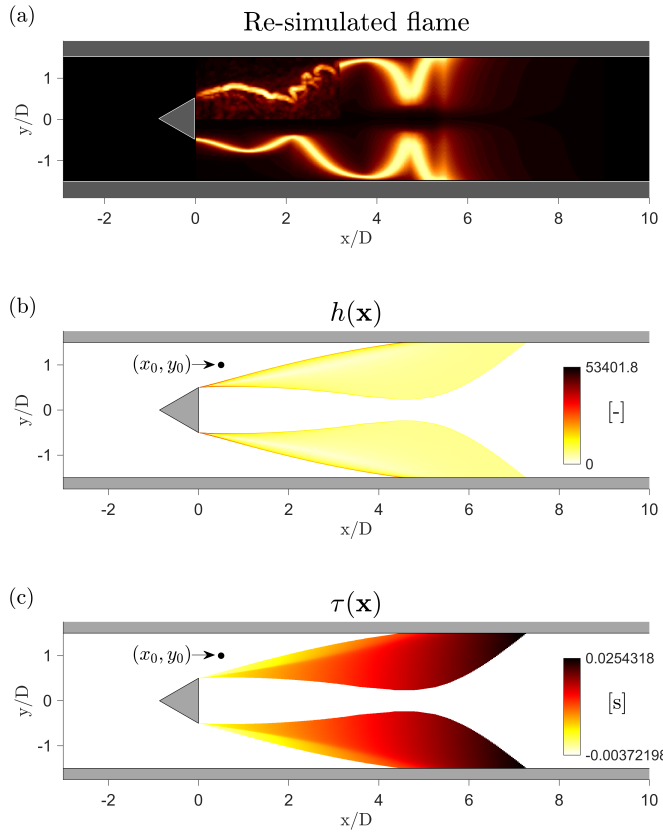
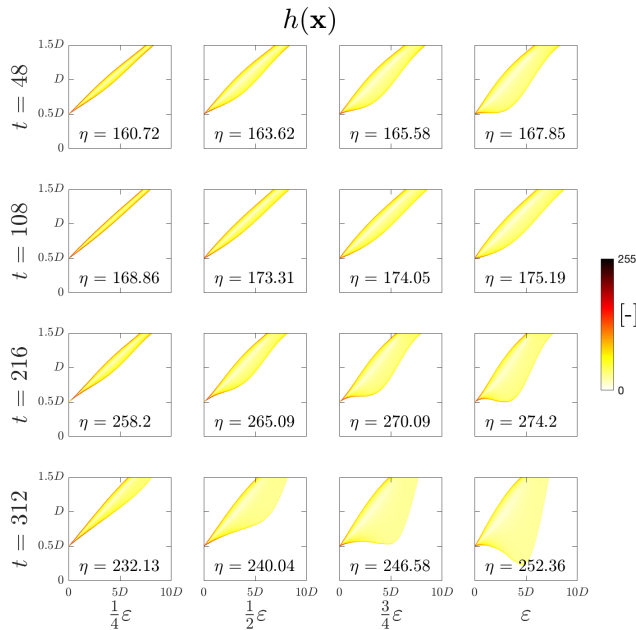FIGURE 9: AS FOR FIG. 6 WITH $t = 312$.

FIGURE 10: DISTRIBUTIONS OF $h(\mathbf{x})$ AT FOUR DIFFERENT TIME STEPS t AND AT FOUR AMPLITUDES: $\varepsilon/4$, $\varepsilon/2$, $3\varepsilon/4$ AND ε. THE VALUES OF η ARE ALSO DISPLAYED FOR EACH TIME STEP AND AMPLITUDE.
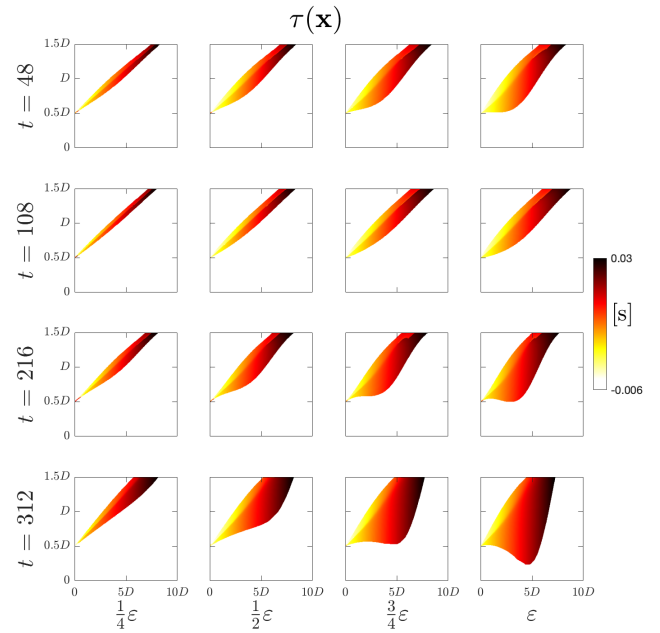

FIGURE 11: DISTRIBUTIONS OF $\tau(\mathbf{x})$ AT THE SAME CONDITIONS AS IN FIG. 10.

in the combustor is modelled by the locally parabolic profile:

$$
T(x, y) = \begin{cases} T_{amb} + \dfrac{T_{peak}}{1 + \left| \dfrac{y}{k_1(m_1 x + n_1)} \right|^{2k_2(m_2 x + n_2)}}, & \text{if } x \geq x_f \\ T_{amb}, & \text{otherwise} \end{cases}
\tag{10}
$$

with parameters $T_{amb} = 300$ K, $T_{peak} = 1700$ K, $k_1 = 0.01905$, $k_2 = 10$, $m_1 = 3.72$, $m_2 = -1.96$, $n_1 = -2.21$, $n_2 = 2.53$. The local speed of sound is taken as $c(x, y) = \sqrt{\gamma R T(x, y)}$ with $\gamma = 1.4$ and is shown in Fig. 12. The mean density field $\rho(x, y)$ is computed from the ideal gas law, $P_{amb} = \rho(x, y) R T(x, y)$. All the boundaries are assumed to be sound-hard (Neumann), apart from the outlet boundary (right-end), where the sound-soft (Dirichlet) boundary condition is imposed.

4.2 Discretization and solution method

The geometric parameters of the domain are taken from the experimental rig in Ref. [27]. The computational grid is generated by Gmsh [37] using Delaunay triangulation. The computational grid consists of 183,222 cells for this two-dimensional planar calculation. The Finite element modelling is implemented in the open-source platform DOLFINx[38] using P1 Galerkin elements [36]. The weak forms are defined using the UFL package [39]. All the matrices are assembled within DOLFINx apart from the active flame matrix. This matrix is implemented using the PETSc package[40]. The EPS solver in the SLEPc package[41] is used to determine the nonlinear quadratic eigenvalue problem, by converting it into a linear eigenvalue problem. The shift-and-invert spectral transformation is exploited to enhance the convergence of the eigenvalue to the initial guess. Fixed point

FIGURE 12: DISTRIBUTIONS OF THE SPEED OF SOUND $c(x, y)$ IN THE THERMOACOUSTIC CALCULATION
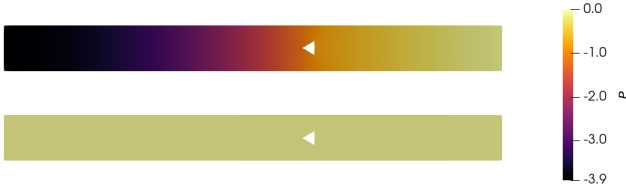

FIGURE 13: REAL (TOP) AND IMAGINARY (BOTTOM) COMPONENTS OF THE ACOUSTIC PRESSURE EIGENFUNCTIONS OF THE 1ST MODE FOR THE FLAME AT $t = 310$ AND AMPLITUDE ϵ_0. THE EIGENFUNCTION IS NORMALIZED SUCH THAT $\int p^2 dx = 1$.
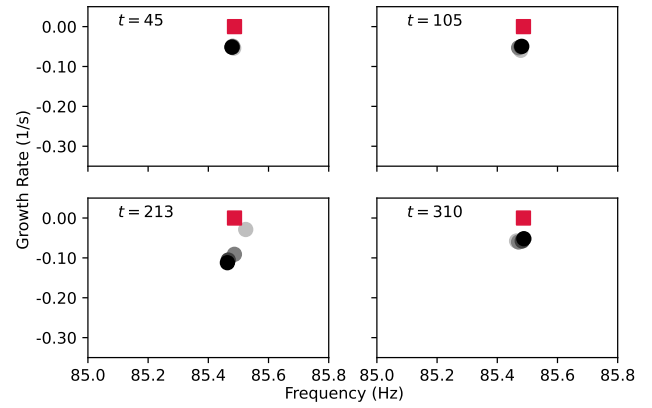

FIGURE 14: THE EIGENVALUES FOR THE 1ST MODE AT FOUR TIMESTEPS AND AMPLITUDES. THE RED SQUARES SHOW THE EIGENVALUE IN THE ABSENCE OF THE THERMOACOUSTIC EFFECT. THE GREY CIRCLES SHOW THE EIGENVALUE AT THE FOUR VALUES OF ε IN TABLE 3. THE LIGHTEST GREY CORRESPONDS TO $\epsilon_0/4$ AND THE DARKEST TO ϵ_0.

iteration with relaxation is implemented in order to converge to the eigenvalue[16].

4.3 Thermoacoustic eigenmodes

Fig 13 shows typical thermoacoustic eigenfunctions for the first thermoacoustic mode. This has the same structure as the natural modes observed experimentally in a similar configuration by [27]. The eigenfunctions at other operating points are nearly identical. Figure 14 shows the first pure acoustic eigenmode (red square) and the thermoacoustic eigenmodes (grey) at the four amplitudes and four timesteps in table 3. The grey symbols deviate from the red square, showing that the thermoacoustic effect is active. At the points examined in this paper, the thermoacoustic effect stabilizes the mode and shifts the frequency slightly.

4.4 Physical interpretation of the thermoacoustic behaviour

The calculations with the Hemholtz solver show that the thermoacoustic frequency and growth rate are only slightly affected by the amplitude of oscillation and the timestep. Table 3 and Figs. 10 to 11 show how η and the n and τ fields vary with the oscillation amplitude and timestep. In this section, we explain the thermoacoustic behaviour with reference to the physics-based heat release rate model.

At a given amplitude, the n field, which describes the shape swept out by the oscillating flame, and η, which describes the global intensity of heat release rate fluctuations, depend significantly on the timestep. This is to be expected because n and η were assimilated from different points in the experimental run, lead to different parameters in LSGEN, and therefore lead to different fluctuating heat release rate fields. At a given timestep, n becomes narrower as the amplitude ϵ reduces, but retains two high amplitude regions: one at the outer edge (the top edge in

Fig. 10) and one at the inner edge (the bottom edge in Fig. 10). On the other hand, η increases only slightly with amplitude. This shows that, once the shape of the flame envelope n has been fixed, the amplitude of the global fluctuating heat release rate depends only slightly on the amplitude of oscillation. This is the expected behaviour because there are two high amplitude regions of n and, once they have been created and separated, the global fluctuating heat release rate η does not depend much on how far apart they are.

The time delay field, τ, becomes narrower as the amplitude reduces and has the same envelope as the n field. The influential region of the τ field is simply the region in which n is large, which is the outer edge of the envelope of n. In this region, the value of τ at a given x-position depends very little on amplitude and only slightly on timestep. This is because τ is determined by the convection speed, K. The small dependence on amplitude is expected because the convection speed of waves down the flame U/K is not affected at all by the amplitude of oscillation, ϵ. The dependence on timestep is also expected to be small because the convection speed is similar at each timestep.

We expect the shape of n to have little influence on the thermoacoustic behaviour because this behaviour is determined by the integral of n multiplied by p over an acoustic wave, and p has a long wavelength. On the other hand, τ/T typically ranges from 0 to 4.5 in the region in which n has high amplitude. Small changes in τ would therefore cause big changes in the phase between q and p, and therefore big changes in the thermoacoustic growth rate, as described in [1]. However, $\tau(x)$ does not change with amplitude or timestep because it is determined by the convection speed, which is the same through the experimental run. The thermoacoustic behaviour is therefore similar at all four timesteps and all four amplitudes.

8

5. CONCLUSIONS

In this paper we assimilate experimental data from a bluff-body-stabilized premixed flame into a physics-based G-equation flame model by finding the parameters of the model that best fit the data. The parameters are recognised using a Bayesian ensemble of Neural Networks (BayNNE) that is trained on 2400 G-equation simulations. The training process is computationally expensive but the assimilation process is cheap and could be performed in real time alongside the experiments. This approach combines the attractive features of physics-based approaches, such as extrapolatability and interpretability, with the attractive features of NNs, such as speed and ease of use. The parameters are assimilated from observations of just the upstream portion of the flame. With the assimilated parameters, the heat release rate is extrapolated everywhere in space over a cycle, using the G-equation flame model. This is repeated at different timesteps and is also extrapolated to lower amplitudes. This extrapolation in physical space and parameter space is achieved with the physics-based model, not with the BayNNE.

The heat release rate fields over a cycle are then converted to a distributed $n - \tau$ model. This is entered into a thermoacoustic Helmholtz solver in order to calculate the frequency and growth rate of thermoacoustic oscillations, given the combustor geometry, temperature, and $n - \tau$ models. We find that the thermoacoustic behaviour is similar for all timesteps and all amplitudes. This result is not surprising when interpreted through the physics-based model: Once the flame starts to oscillate, there are two high amplitude regions in the n field. The time delay, τ, in these high amplitude regions could have a strong influence on the thermoacoustic behaviour because τ is, in places, several multiples of the acoustic period, T [1]. The value of τ in these high amplitude regions is, however, similar at all timesteps and amplitudes. This is because τ is determined by the perturbation convection speed, which is the same at all timesteps and amplitudes.

The experiment exhibits intermittent bouts of thermoacoustic oscillations around the fundamental frequency, which is consistent with a lightly-damped oscillator being forced by noise. These results are consistent with the thermoacoustic model predictions, which were based on the flame behaviour assimilated while the system was oscillating. The data comes from a single experimental run so it is difficult to draw any further conclusions about the thermoacoustic behaviour other than that the experimental data and the model behaviour are consistent with each other.

Nevertheless, the assimilation process itself has proven to be useful. During moments of intermittent oscillation, the BayNNE can successfully identify the parameters of a physics-based model of the flame that matches the data. Because the model is physics-based, it can extrapolate in physical space (i.e. beyond the observation window) and in parameter space (in this case to lower amplitudes) to obtain distributed heat release rate models that can be used successfully in a thermoacoustic model.

As increasingly large quantities of experimental data become available, we need to extract useful information without becoming overwhelmed. Assimilation into physics-based models, as performed here, is attractive because the models are physically-interpretable and extrapolatable. Firstly, this provides a cheap way to store CFD data - e.g. the parameters of the most relevant CFD solution for a given experiment can be extracted cheaply, and the CFD solution then re-calculated. Secondly, this shows how sparse experimental results can be combined with numerical results to extrapolate, with defined confidence levels, beyond experimental observations. This paper described a robust way and potentially cheap method to achieve this, which can readily be extended to other experiments and to other models.

REFERENCES

[1] Juniper, Matthew P. and Sujith, R. I. "Sensitivity and non-linearity of thermoacoustic oscillations." *Annual Review of Fluid Mechanics* Vol. 50 (2018): pp. 661–689. DOI 10.1146/annurev-fluid-122316-045125.

[2] MacKay, David J. C. *Information Theory, Inference, and Learning Algorithms.* Cambridge University Press (2003).

[3] Sengupta, Ushnish, Rasmussen, Carl E. and Juniper, Matthew P. "Bayesian machine learning for the prognosis of combustion instabilities from noise." *Journal of Engineering for Gas Turbines and Power* Vol. 143 (2017).

[4] McCartney, Michael, Sengupta, Ushnish and Juniper, Matthew P. "Reducing uncertainty in the onset of combustion instabilities using dynamic pressure information and bayesian neural networks." *Journal of Engineering for Gas Turbines and Power* Vol. 144 . DOI 10.1115/1.4052145/1115809.

[5] Waxenegger-Wilfing, Günther, Sengupta, Ushnish, Martin, Jan, Armbruster, Wolfgang, Hardi, Justin, Juniper, Matthew P. and Oschwald, Michael. "Early detection of thermoacoustic instabilities in a cryogenic rocket thrust chamber using combustion noise features and machine learning." *Chaos (Woodbury, N.Y.)* Vol. 31 . DOI 10.1063/5.0038817.

[6] Juniper, Matthew P. and Yoko, Matthew. "Generating a physics-based quantitatively-accurate model of an electrically-heated Rijke tube with Bayesian inference." *Journal of Sound and Vibration* Vol. 535 (2022): p. 117096. DOI 10.1016/J.JSV.2022.117096.

[7] Yu, Hans, Juniper, Matthew P. and Magri, Luca. "A data-driven kinematic model of a ducted premixed flame." *Proceedings of the Combustion Institute* Vol. 38 (2021): pp. 6231–6239. DOI 10.1016/j.proci.2020.06.137.

[8] Rayleigh, John W. S. B. "The explanation of certain acoustical phenomena." *Nature* Vol. 18 (1878): pp. 319–321.

[9] Lieuwen, Tim. "Unsteady Combustor Physics." *Unsteady Combustor Physics* DOI 10.1017/9781108889001.

[10] Smart, A., Jones, B. and Jewell, N. "Measurements of unsteady parameters in a rig designed to study reheat combustion instabilities." DOI 10.2514/6.1976-141.

[11] Pitz, Robert W. and Daily, John W. "Combustion in a turbulent mixing layer formed at a rearward-facing step." *AIAA Journal* Vol. 21 (1983): pp. 1565–1570. DOI 10.2514/3.8290.

[12] Smith, D. A. and Zukoski, E. E. "Combustion instability sustained by unsteady vortex combustion." *undefined* (1985)DOI 10.2514/6.1985-1248.

[13] Poinsot, T., Trouve, Arnaud C., Veynante, Denis P., Candel, Sebastien M. and Esposito, Emile J. "Vortex-driven acoustically coupled combustion instabilities." *Journal of Fluid Mechanics* Vol. 177 : pp. 265–292. DOI 10.1017/S0022112087000958.

[14] Crocco, Luigi. "Research on combustion instability in liquid propellant rockets." *Symposium (International) on Combustion* Vol. 12 (1969): pp. 85–99. DOI 10.1016/S0082-0784(69)80394-2.

[15] Williams, Forman A. "Turbulent combustion." DOI 10.1137/1.9781611971064.CH3.

[16] Nicoud, F., Benoit, L., Sensiau, C. and Poinsot, T. "Acoustic modes in combustors with complex impedances and multi-dimensional active flames." *AIAA Journal* Vol. 45 . DOI 10.2514/1.24933.

[17] Caswell, Andrew W., Rankin, Brent A., Huelskamp, Bethany C., Lynch, Amy C., Belovich, Vincent and Gord, James R. "Spatiotemporal characterization of bluff-body stabilized turbulent premixed flames using simultaneous high-repetition-rate OH PLIF and PIV measurements." *53rd AIAA Aerospace Sciences Meeting* (2015): pp. 1–12DOI 10.2514/6.2015-0424.

[18] Evensen, G. "Sequential data assimilation with a nonlinear quasi-geostrophic model using Monte Carlo methods to forecast error statistics." *Journal of Geophysical Research* Vol. 99 : pp. 10143–10162. DOI 10.1029/94jc00572.

[19] Yu, Hans, Juniper, Matthew P. and Magri, Luca. "Combined state and parameter estimation in level-set methods." *Journal of Computational Physics* Vol. 399 : pp. 1–51. DOI 10.1016/j.jcp.2019.108950.

[20] Yu, Hans. "Inverse Problems in Thermoacoustics." (2020).

[21] Gal, Yarin and Ghahramani, Zoubin. "Dropout as a Bayesian approximation: representing model uncertainty in deep learning." 2016. WCP.

[22] Pearce, Tim, Leibfried, Felix, Brintrup, Alexandra, Zaki, Mohamed and Neely, Andy. "Uncertainty in neural networks: approximately Bayesian ensembling." Vol. 108.

[23] Sengupta, Ushnish, Croci, Maximilian L. and Juniper, Matthew P. "Real-time parameter inference in reduced-order flame models with heteroscedastic Bayesian neural network ensembles." 2020.

[24] Sengupta, Ushnish, Amos, Matt, Hosking, J. Scott, Rasmussen, Carl E., Juniper, Matthew P. and Young, Paul J. "Ensembling geophysical models with Bayesian neural networks." 2020.

[25] Croci, Maximilian L., Sengupta, Ushnish and Juniper, Matthew P. "Online parameter inference for the simulation of a Bunsen flame using heteroscedastic Bayesian neural network ensembles." 2021.

[26] Croci, Maximilian L., Sengupta, Ushnish and Juniper, Matthew P. "Data assimilation using heteroscedastic Bayesian neural network ensembles for reduced-order flame models." *Lecture Notes in Computer Science (including subseries Lecture Notes in Artificial Intelligence and Lecture Notes in Bioinformatics)* Vol. 12746 LNCS (2021): pp. 408–419. DOI 10.1007/978-3-030-77977-1_33.

[27] Fugger, C. A., Yi, Tongxun, Sykes, Joshua P., Caswell, Andrew W., Rankin, Brent A., Miller, Joseph D. and Gord, James R. "The structure and dynamics of a bluff-body stabilized premixed reacting flow." *AIAA Aerospace Sciences Meeting* (2018)DOI 10.2514/6.2018-1190.

[28] Kiel, Barry, Garwick, Kyle, Gord, James R., Miller, Joseph D., Lynch, Amy C., Hill, Roger and Phillips, Scott. "A detailed investigation of bluff body stabilized flames." *Collection of Technical Papers - 45th AIAA Aerospace Sciences Meeting* Vol. 3 : pp. 2019–2028. DOI 10.2514/6.2007-168.

[29] Kiel, Barry, Garwick, Kyle, Lynch, Amy C., Gord, James R. and Meyer, Terrence. "Non-reacting and combusting flow investigation of bluff bodies in cross flow." *Collection of Technical Papers - AIAA/ASME/SAE/ASEE 42nd Joint Propulsion Conference* Vol. 11 : pp. 8743–8753. DOI 10.2514/6.2006-5234.

[30] Kashinath, Karthik, Li, Larry K.B. and Juniper, Matthew P. "Forced synchronization of periodic and aperiodic thermoacoustic oscillations: Lock-in, bifurcations and open-loop control." *Journal of Fluid Mechanics* Vol. 838 (2018): pp. 690–714. DOI 10.1017/JFM.2017.879.

[31] Hemchandra, Santosh. "Dynamics of Turbulent Premixed Flames in Acoustic Fields." (2009).

[32] Lakshminarayanan, Balaji, Pritzel, Alexander and Blundell, Charles. "Simple and scalable predictive uncertainty estimation using deep ensembles." 2017.

[33] He, Siyu, Li, Yin, Feng, Yu, Ho, Shirley, Ravanbakhsh, Siamak, Chen, Wei and Póczos, Barnabás. "Learning to predict the cosmological structure formation." *Proceedings of the National Academy of Sciences of the United States of America* Vol. 116 (2019): pp. 13825–13832. DOI 10.1073/PNAS.1821458116.

[34] Juniper, Matthew P. "Sensitivity analysis of thermoacoustic instability with adjoint Helmholtz solvers." *Physical Review Fluids* Vol. 3 (2018). DOI 10.1103/PhysRevFluids.3.110509.

[35] Herráez, Miguel Arevallilo, Burton, David R., Lalor, Michael J. and Gdeisat, Munther A. "Fast two-dimensional phase-unwrapping algorithm based on sorting by reliability following a noncontinuous path." *Applied optics* Vol. 41 : p. 7437. DOI 10.1364/AO.41.007437.

[36] Falco, Stefano. "Shape optimization for thermoacoustic instability with an adjoint Helmholtz solver." DOI 10.17863/CAM.84402.

[37] Geuzaine, C. and Remacle, J. "Gmsh : a three-dimensional finite element mesh generator with built-in pre-and post-processing facilities." (2009).

[38] Logg, Anders and Wells, Garth N. "DOLFIN." *ACM Trans-*

actions on Mathematical Software (TOMS) Vol. 37 . DOI
10.1145/1731022.1731030.

[39] Alnæs, Martin S., Logg, Anders, Ølgaard, Kristian B., Rognes, Marie E. and Wells, Garth N. "Unified form language: A domain-specific language for weak formulations of partial differential equations." *ACM Transactions on Mathematical Software (TOMS)* Vol. 40 : p. 1. DOI 10.1145/2566630.

[40] Balay, S., Abhyankar, S., Adams, M., Brown, J., Brune, P., Buschelman, K., Dalcin, L., Dener, A., Eijkhout, V., Gropp, W., Karpeyev, D., Kaushik, D., Knepley, M., May, D., McInnes, L. Curfman, Mills, R., Munson, T., Rupp, K., Sanan, P., Smith, B., Zampini, S., Zhang, H. and Zhang, H. "PETSc Users Manual: Revision 3.11." DOI 10.2172/1577437.

[41] Hernandez, Vicente, Roman, Jose E. and Vidal, Vicente. "SLEPc: A scalable and flexible toolkit for the solution of eigenvalue problems." *ACM Transactions on Mathematical Software (TOMS)* Vol. 31 (2005): pp. 351–362. DOI 10.1145/1089014.1089019.